Survey and Continuous GNSS in the vicinity of the July 2019 Ridgecrest earthquakes

Michael Floyd[1,*], *Gareth Funning*[2], *Yuri Fialko*[3], *Rachel Terry*[2,†], *Thomas Herring*[1]

[1] Department of Earth, Atmospheric and Planetary Sciences, Massachusetts Institute of Technology, Cambridge, Massachusetts, USA
[2] Department of Earth Sciences, University of California, Riverside, California, USA
[3] Scripps Institution of Oceanography, University of California, San Diego, California, USA
† Now at UNAVCO, Inc., Boulder, Colorado, USA
* Corresponding author

Abstract

The M_w6.4 and M_w7.1 Ridgecrest, California, earthquakes of July 2019 occurred within 34 hours of each other on conjugate strike-slip faults in the Mojave Desert, just north of the central Garlock Fault. Here we present the results of a survey of 18 Global Navigation Satellite Systems (GNSS) sites conducted in the immediate aftermath of the earthquakes, including five sites which recorded the motion of the second earthquake, after having been set up immediately following the first, as well as processed results from continuous GNSS sites throughout the region. Our field work in response to the earthquakes provides additional constraints on the ground displacement due to both earthquakes, complementing data from a spatially sparser network of continuously recording GNSS sites in the area, as well as temporally sparser Interferometric Synthetic Aperture Radar (InSAR) data that were able to capture a combined deformation signal from the two earthquakes.

1. Introduction

The pair of large earthquakes near Ridgecrest, California, in July 2019—an M_w6.4 event on July 4th and an M_w7.1 event on July 5th, local time (July 6th, Universal Time)—occurred 34 hours apart in a region with a number of geodetic monuments with many years of archived Global

Navigation Satellite Systems (GNSS), specifically Global Positioning System (GPS), survey data. The earthquakes occurred on conjugate faults in a region of active deformation and seismicity in the Eastern California Shear zone, and in proximity to the Coso geothermal field and to the Garlock Fault, both of which had been targets for study in these earlier GNSS surveys, in the 1990s and early 2000s (e.g., McClusky et al., 2001; Miller et al., 2001a; Figure 1; Table 1).

In more recent years, some of these survey sites were reoccupied with GNSS equipment, in order to improve uncertainties of the secular velocities at those sites (e.g., Funning et al., 2019a). These recent surveys, and the knowledge gained from them, facilitated a rapid response to the first Ridgecrest earthquake (and therefore to the second earthquake as well), enabling the separation of the coseismic displacements of the two events. Additional, and ongoing, survey measurements made in the days following the second, M_w7.1 earthquake will enable the study of postseismic deformation due to the Ridgecrest events. When combined with data from continuous GNSS stations in the region, from the Network of the Americas (NOTA) operated as part of the Geodesy Advancing Geoscience and EarthScope (GAGE) facility at UNAVCO, as well as stations operated by the United States Geological Survey (USGS), they provide a detailed picture of the Ridgecrest events and their aftermath. In contrast to Interferometric Synthetic Aperture Radar (InSAR) measurements of the coseismic displacements, which can only constrain the total displacement from the two earthquakes and the first few days of postseismic response (e.g., Fielding et al., 2019; Wang and Bürgmann, 2019; Xu and Sandwell, 2019), the available GNSS data can measure coseismic displacements due to the M_w6.4 and M_w7.1 events individually, as well as separate coseismic signals from any postseismic deformation. As such, they provide a useful resource for researchers interested in constraining models of coseismic slip or postseismic response, in addition to providing a foundation for potential future investigations regarding fault interactions and stress transfer.

In this study, we describe the archived survey data sets from the region, the survey response to the Ridgecrest earthquakes, and present a new, combined solution from both survey and continuous GNSS sites for the displacements during the Ridgecrest earthquakes.

2. Previous surveys and velocity solutions

Surveys throughout the Mojave Desert in the region of the Garlock Fault were conducted mostly in the 1990s and early 2000s (see Table 1). These focused on two aspects of the region, the relative motion of faults, including the Garlock Fault, throughout the Eastern California Shear Zone (ECSZ) from the California-Nevada state line in the northeast to the San Andreas Fault in the southwest, and the deformation of the Coso geothermal field where the geothermal energy production is associated with subsidence at a rate of a few centimeters per year (e.g., Fialko and Simons, 2000; Tymofyeyeva and Fialko, 2015). The GNSS survey results related to the former were presented by Miller et al. (2001) and McClusky et al. (2001). The latter study inferred a strike-slip motion across the Airport Lake Fault (the previously-mapped fault most closely, although not exactly, associated with the M_w7.1 Ridgecrest earthquake) to be 5.7 ± 0.7 mm/yr. Shen et al. (2011) presented a rigorous reprocessing and combination of surveys throughout California for the Southern California Earthquake Center (SCEC) Crustal Motion Map (CMM) (Figure 1; blue vectors and circles). The region also contains a network of continuously operating sites (Figure 1; red vectors and circles), which are processed routinely and derived products such as velocity solutions are generated and available publicly from UNAVCO. The continuous velocity solution shown in Figure 1 is that of Herring et al. (2018a).

The profile shown in Figure 1b across this latest velocity solution shows a similar velocity gradient across the region, although we do not model it explicitly using elastic dislocations here to update the model of McClusky et al. (2001).

In more recent years, a group from the University of California, Riverside (UCR) conducted a survey in 2014 which mostly covered the southern and eastern Mojave Desert, but also measured a couple of sites (HAW0 and LNWD) further north in the Mojave, to the southwest of the July 2019 earthquakes (Funning, 2016). In addition to site occupations, the group conducted extensive site reconnaissance, that was leveraged for later visits.

The most recent pre-earthquake surveys were conducted in February and March 2019, again by a group from UCR. As part of a project funded by SCEC to update deformation velocities in the Mojave desert region, 21 sites were occupied for durations of between 17 and 26 hours each (Figure S1), including a transect of the Garlock Fault southwest of Ridgecrest.

3. Survey response to the July 2019 earthquakes

A field team from UCR responded promptly to the July 4th event, arriving in the field in the afternoon. On the afternoon of July 4th and morning of July 5th, we occupied four sites to the west and southwest of the epicenter (H701, J701, F048 and ATOL) that had previously been measured in February 2019, as well as one site to the south (PNCL) that had been measured in 2001. The first of these measurements were started within seven hours of the M_w6.4 earthquake, with all five sites operating within 30 km of the rupture within 26 hours (see Figure S2). All five remained standing and running during and after the second, M_w7.1 earthquake that occurred 34 hours after the M_w6.4, providing a unique, near-field constraint on the deformation from each event separately; as we will show below, site PNCL, fortuitously located only 600 m from the surface rupture of the M_w7.1 event, detected the highest displacements—over 80 cm of horizontal displacement in the M_w7.1 earthquake.

In the days that followed the two events, multiple additional sites were occupied in the epicentral region by groups from Scripps Institute of Oceanography (SIO), the University of Nevada, Reno (UNR) and the USGS, as well as by UCR. Coordination between these groups enabled an efficient field response, maximizing coverage while minimizing duplication of effort. Given the difficulties of obtaining access to the Navy Air Weapons Station (NAWS) China Lake (see Figure 1), within which the majority of the surface ruptures occurred, the effort from UCR, SIO and UNR focused on the area outside of the NAWS, leaving the responsibility of occupying sites within the NAWS to the USGS (Brooks et al., 2019). By the end of July 9th, local time, 19 survey sites had been occupied by UCR (yellow triangles in Figures 2, 3 and 4), SIO (green triangles in Figure 3 and 4) and UNR combined, and a further 13 sites, including 8 stations forming 4 cross-fault arrays targeted at detecting shallow afterslip, had been installed by the USGS (Brooks et al., 2019). Some of the monuments are metal rods cemented in competent rocks, occupied with a GNSS antenna mounted on a tripod, while others involve a concrete block with a threaded metal rod on which an antenna could be attached directly, without the need for a tripod (see Figure S3 for several examples). Each of the survey sites recorded data at a standard low rate (e.g., 15 or 30 seconds) for daily processing, using an Ashtech Z-12, Septentrio PolaRx5, Topcon GB-1000 or Trimble R7, NetRS or NetR9 receiver with an Ashtech Choke Ring, Topcon PG-A1 or Trimble Geodetic L1/L2 Compact, Zephyr Geodetic or Zephyr Geodetic 2 antenna.

With additional deployments in the days and weeks that followed, by September 7th 27 sites had been occupied by UCR, SIO and UNR, and a further 16 by the USGS, the majority of these in a "semi-continuous" mode (e.g., Blewitt et al., 2009), whereby the stations are powered to run for weeks at a time, and infrequently serviced to retrieve data, check the centering of antennas, and perform maintenance. The majority of these semi-continuous stations will be operated into 2020, in order to capture details of any postseismic transient motion following the earthquakes. High-rate data during the earthquakes themselves is available for most of the continuous sites in the region operated by UNAVCO (Mattioli et al., 2019, UNAVCO Community, 2019).

4. GNSS processing

The solutions were processed using a pre-release version of GAMIT/GLOBK 10.71 (update of Herring et al., 2018b). The results of the surveys were then combined with processed solutions for continuous sites from the Network of the Americas (NOTA) within the surrounding region. These solutions differ slightly from the official GAGE solutions in that they were split on the days of the earthquakes to avoid artifacts in the time series, where the usual 00:00 GPST (GPS Time) to 00:00 GPST processing day straddles a major displacement, resulting in a time series points which "hangs" at a weighted average between the positions before and after the earthquake on the day of the event itself.

The data from the continuously running GNSS receivers in the region were processed for the period between July 2nd (day 183) and July 9th (day 190), 2019, in nominally 24-hour sessions. On the days of the earthquakes, the 24-hour sessions were divided into two sessions. The first session ran from 00:00 GPST to the minute before the earthquake on that day and the second session started 5 minutes after the earthquake origin time and finished at 23:59:30 GPST. The processing was carried out in eight sub-networks each containing 66 to 67 stations. The 507 stations processed spanned a region about twice the diameter of the area likely to have undergone more than 1 mm of the coseismic displacement from the July 6th M_w7.1 event. The satellite orbits were fixed to the International GNSS Service (IGS) global orbits. The division of the networks and the processing of the data followed that same approach described for the GAMIT processing in Herring et al. (2016). The realization of the reference frame was the same as that described in Herring et al. (2016) but the newer North America 2014 (NAM14) was used. The positions, velocities and reference frame sites for NAM14 are available from UNAVCO (ftp://data-out.unavco.org/pub/products/velocity/pbo.final_nam14.vel).

The data from the survey sites (five yellow triangles in Figures 2–4) were set up from July 5th (day 186) onwards (see Figure S2), therefore capturing the second earthquake. The sites were processed in one session for the 27 hours between their deployment and the second earthquake at 03:12 UTC on 2019-07-06 (day 187), for the 21 hours remaining after the earthquake on 2019-07-06, and for standard 24-hour UTC-day sessions thereafter. These results were then combined with the similarly-arranged sessions from the processing of continuous sites.

Four of the survey sites had been measured previously during the February and March 2019 surveys (Funning et al., 2019a; see Section 2) but did not have enough previous data to determine a velocity before the earthquake. We therefore assumed, in the four to five months between their first observation and the first earthquake (Funning et al., 2019b), motion consistent with a velocity constrained to within 0.5 mm/yr of nearby continuous site RAMT for survey site ATOL; of the mean velocity of nearby continuous sites CCCC and P616, whose velocities are within 1 mm/yr of each other, for survey sites F048, H701 and J701; and of the mean velocity of nearby continuous sites CCCC, P580 and P595 for survey site PNCL. This allowed us to estimate displacements at these sites during the first earthquake also. Furthermore, we similarly constrained the pre-earthquake velocity for a few survey sites with imprecise estimates due to short or few previous observations: 0806 was constrained in the same way as ATOL, above; survey site INYO in the same way as F048, H701 and J701, above; and V511 to the velocity of nearby survey site BM25. This allowed us to estimate cumulative displacements at these sites due to both earthquakes combined, having been observed again only after the second earthquake.

We processed all data from previous surveys that contained data from sites occupied in the aftermath of the earthquakes (see Table S1). We also include the results from McClusky et al. (2001) by incorporating their full solution and associated covariance matrix during combination of the survey and one-week continuous results.

5. Results

Figures 2, 3 and 4 show the estimated displacements after combination of the continuous and survey solutions described in Section 4, above, for the first M_w6.4 earthquake, the second M_w7.1 earthquake and the two earthquakes combined, respectively. Unfortunately, many of the sites occupied immediately after the earthquakes (triangles in Figures 3 and 4) do not have sufficient data beforehand to allow reasonable estimation of coseismic displacements from prior observations alone. Many of them were last measured briefly around the time of the 1999 Hector Mine earthquake, and therefore are subject not only a long period (20 years) of no observations but also short, segmented time series and perturbed tectonic velocities, both leading to poorly constrained pre-earthquake velocities. Nevertheless, we explain our approach to constraining their pre-earthquake velocities, and therefore coseismic displacements, in Section 4, above.

Four survey sites to the west and south of the first, M_w6.4 earthquake help constrain the displacements in a region where only two nearby continuous sites otherwise exist in the near-field (Figure 3). The same four survey sites help constrain the southern west side of the second, M_w7.1 earthquake, as well as PNCL at the very southern end of the rupture.

The displacements for the M_w6.4 earthquake (Figure 2) are consistent with a predominantly left-lateral rupture, as we observed in the immediate aftermath of the earthquake. The closest sites to the rupture show displacements of 3 cm and 11 cm (at H701 and P595, respectively) that are oriented oblique to the strike of the fault, a consequence of their locations beyond the ends of the rupture, and in keeping with the expected deformation pattern for a finite left-lateral strike-slip fault. For the M_w7.1 earthquake (Figure 3), we observe a clear right-lateral displacement pattern overall, consistent with the north-west strike of the mapped ruptures in the area, with fault-parallel displacements at sites located within a zone perpendicular to the major surface rupture and rotation of the displacement vectors at sites beyond the ends of the rupture. The largest recorded displacements of approximately 80 cm are at survey site PNCL, with a trend that is subparallel to the local fault strike.

6. Summary

We present a coseismic displacement solution for combined continuous and survey GNSS, for both the M_w6.4 and M_w7.1 July 2019 Ridgecrest earthquakes separately and combined. To obtain these results, we reprocessed previous surveys from the 1990s and 2000s, as well as presenting more recent surveys from February and March 2019 to the west and south of the Ridgecrest ruptures. These results help to constrain particularly the separate ground displacements, as well as eventually the continuing post-earthquake motions, if any, after more observations continue to be made at the same GNSS sites. All post-earthquake survey data collected by UCR and SIO/UCSD are archived at UNAVCO, which will be supplemented as further surveys are conducted.

We recommend that, for the purposes of earthquake response, GNSS surveys remain a vital component of geodetic observations that should be undertaken regularly to avoid long gaps in time series, which decrease the precision of eventual pre-earthquake positions and may also be contaminated by otherwise unobserved non-secular velocity perturbations. We also suggest that the processed solutions (e.g., Solution Independent Exchange format; SINEX) for previous surveys be made readily available, in addition to the raw (e.g., Receiver-Independent Exchange format; RINEX) data currently archived on a routine basis by working groups. When the need for rapid response arises, well-informed field teams are required to target sites which are going to produce the best coseismic and post-earthquake measurements. Furthermore, we recommend that post-earthquake surveys are conducted at high rates of observation (i.e., greater than 1 Hz frequency) for potential seismogeodetic studies in the case of large aftershocks or, as in the case of the Ridgecrest earthquakes, a larger secondary earthquake, although such an approach does proportionally increase the burden of regular recovery of data on field teams to conserve receiver disk storage.

Data and Resources

Table 1 contains a list of surveys processed for this work, each of which are available from UNAVCO via the digital object identifiers (DOIs) in the final column. Additional RINEX files processed for this work are available from the USGS via the Northern California Earthquake Data Center (NCEDC; ftp://ftp.ncedc.org/pub/gps/survey/usgs/) and from SCEC via the Southern California Earthquake Data Center (SCEDC; https://service.scedc.caltech.edu/gps/). Table S1 contains the coseismic displacements estimated due to the first, M_w6.4 earthquake, shown in Figure 2. Table S2 contains the coseismic displacements estimated due to the second, M_w7.1 earthquake, shown in Figure 3. Table S3 contains the cumulative coseismic displacements estimated due to both earthquakes combined, shown in Figure 4.

Acknowledgements

This paper is dedicated to Meghan M. Miller, on her retirement as President of UNAVCO, upon whose foresight and data collection this study is built. Keith Richards-Dinger, Baoning Wu, Christos Kyriakopolous, Jordan Cortez, John Conrad, Lisa Knowles and Filiz Duda are thanked for assistance in the field. Duncan Agnew is thanked for his timely advice on possible survey targets in the aftermath of the earthquakes. We also thank Ronni Grapenthin and Tony Lowry for their reviews, which greatly improved the manuscript. This material is based on services provided by the GAGE Facility, operated by UNAVCO, Inc., with support from the National Science Foundation and the National Aeronautics and Space Administration under NSF Cooperative Agreement EAR-1724794. This research was supported by the Southern California Earthquake Center (Contribution No. 9995), Awards 14189 (Funning), 18201 (Funning and Terry) and 19106 (Floyd); and by NSF RAPID Awards 1945728 (Funning) and 1945760 (Fialko). SCEC is funded by NSF Cooperative Agreement EAR-1600087 & USGS Cooperative Agreement G17AC00047. This is SCEC contribution #9995.

References

Altamimi, Z., L. Métivier, P. Rebischung, H. Rouby, and X. Collilieux (2017). *ITRF2014 plate motion model*, Geophys. J. Int. **209** 1906–1912, doi:10.1093/gji/ggx136.

Bevis, M., and K. Hudnut (2005a). *GeoEarthScope ALS San Andreas Fault (B4) - 2005-B4-Phase 1*, UNAVCO, Inc., GPS/GNSS Observations Dataset, doi:10.7283/V5MV-QE58.

Bevis, M., and K. Hudnut (2005b). *GeoEarthScope ALS San Andreas Fault (B4) - 2005-B4-Phase 2*, UNAVCO, Inc., GPS/GNSS Observations Dataset, doi:10.7283/FQ3X-X311.

Blewitt, G., W. C. Hammond, and C. Kreemer (2009). Geodetic observation of contemporary deformation in the northern Walker Lane: 1. Semipermanent GPS strategy, in *Late Cenozoic Structure and Evolution of the Great Basin-Sierra Nevada Transition*, John S. Oldow and Patricia H. Cashman (Editors), Special Paper 447, Geological Society of America (GSA), Boulder, CO.

Brooks, B. A., J. Murray, J. Svarc, E. Phillips, R. Turner, M. Murray, T. Ericksen, K. Wang, S. E. Minson, R. Burgmann, F. Pollitz, K. Hudnut, E. A. Roeloffs, J. Hernandez, and B. Olson (2019). *Rapid Geodetic Observations of Spatiotemporally Varying Postseismic Deformation Following the Ridgecrest Earthquake Sequence: The US Geological Survey Response*, Seismol. Res. Lett., in review.

Fialko, Y., and M. Simons (2000). *Deformation and seismicity in the Coso geothermal area, Inyo County, California: Observations and modeling using satellite radar interferometry*, J. Geophys. Res. Solid Earth **105** 21781–21794, doi:10.1029/2000JB900169.

Fialko, Y., Z. Jin, E. Tymofyeyeva, D. T. Sandwell, J. Haase, and M. A. Floyd (2019a). *Ridgecrest California Earthquake Response 2019*, UNAVCO, Inc., GPS/GNSS Observations Dataset, doi:10.7283/N74Q-GA66.

Fialko, Y, Z. Jin, E. Tymofyeyeva, D. T. Sandwell, J. Haase, and M. A. Floyd (2019b). *Ridgecrest California Earthquake Post-Event Response July 2019 UCSD*, UNAVCO, Inc., GPS/GNSS Observations Dataset, doi:10.7283/YJK0-B215.

Fielding, E. J., Z. Liu, O. Stephenson, M. Zhong, C. Liang, A. Moore, S. Yun, and M. Simons (2019). *Surface deformation related to the 2019 Mw 7.1 and Mw 6.4 Ridgecrest earthquakes in California from GPS, SAR interferometry, and SAR pixel offsets*, Seismol. Res. Lett., submitted.

Funning, G. (2016). *San Jacinto Fault 2014*, UNAVCO, Inc., GPS/GNSS Observations Dataset, doi:10.7283/T57H1GZW.

Funning, G., R. Terry, and M. A. Floyd (2019a). *SCEC Mojave 2019*, UNAVCO, Inc., GPS/GNSS Observations Dataset, doi:10.7283/TFX5-EJ21.

Funning, G., C. Kyriakopoulos, B. Wu, K. Richards-Dinger, J. Cortez, and M. A. Floyd (2019b). *Ridgecrest California Earthquake Response 2019*, UNAVCO, Inc., GPS/GNSS Observations Dataset, doi:10.7283/5ASB-9V26.

Herring, T. A., M. A. Floyd, R. W. King (2018a). *GAGE Processing GPS Plate Boundary Observatory Expanded Analysis Product for 2017: Final (Annual) Velocity Field; Combination in Nab08 (IGb08 Rotated into the North America Frame) Reference Frame Using Kalman Filter Analysis of SINEX files from CWU, NMT and PBO Produced by the Massachusetts Institute of Technology (Analysis Center Coordinator)*, UNAVCO, Inc., GPS/GNSS-Based Geodetic Derived Data Product, doi:10.7283/P2GT0N.

Herring, T. A., R. W. King, M. A. Floyd, and S. C. McClusky (2018b). Introduction to GAMIT/GLOBK, Release 10.7, Massachusetts Institute of Technology, Cambridge, http://geoweb.mit.edu/gg/Intro_GG.pdf.

Mattioli, G. S., D. A. Phillips, K. M. Hodgkinson, C. Walls, D. J. Mencin, B. A. Bartel, D. J. Charlevoix, C. Crosby, M. J. Gottlieb, B. Henderson, W. Johnson, D. Maggert, D. Mann, C. M. Meertens, J. Normandeau, J. Pettit, C. M. Puskas, L. Rowan, C. Sievers, and A. Zaino (2019). *The GAGE data and field response to the 2019 Ridgecrest earthquake sequence*, Seismol. Res. Lett., in review.

McClusky, S. C., S. C. Bjomstad, B. H. Hager, R. W. King, B. J. Meade, M. M. Miller, F. C. Monastero, and B. J. Souter (2001). *Present Day Kinematics of the Eastern California Shear Zone from a Geodetically Constrained Block Model*, Geophys. Res. Lett. **28** 3369–3372, doi:10.1029/2001GL013091.

Miller, M. M., M. P. Golombek, and R. K. Dokka (1997). *Mammoth/Mojave 1994*, UNAVCO, Inc., GPS/GNSS Observations (Aggregation of Multiple Datasets), doi:10.7283/T57H1GGM.

Miller, M. M., E. Humphreys, R. K. Dokka, and F. H. Webb (1995). *Mojave 1995*, UNAVCO, Inc., GPS/GNSS Observations Dataset, doi:10.7283/T5H12ZX8.

Miller, M. M., D. J. Johnson, T. H. Dixon, and R. K. Dokka (2001a). *Refined kinematics of the Eastern California shear zone from GPS observations, 1993-1998*, J. Geophys. Res. Solid Earth **106** 2254–2263, doi:10.1029/2000JB900328.

Miller, M. M., E. Humphreys, R. K. Dokka, and F. H. Webb (2001b). *Garlock 1997*, UNAVCO, Inc., GPS/GNSS Observations Dataset, doi:10.7283/T55Q4T1H.

Miller, M. M., E. Humphreys, R. K. Dokka, and F. H. Webb (2001c). *Mojave 1997*, UNAVCO, Inc., GPS/GNSS Observations Dataset, doi:10.7283/T5W66HPD.

Miller, M. M., E. Humphreys, R. K. Dokka, and F. H. Webb (2001d). *Garlock 1998 06 (Jun)*, UNAVCO, Inc., GPS/GNSS Observations Dataset, doi:10.7283/T51Z4295.

Miller, M. M., E. Humphreys, R. K. Dokka, and F. H. Webb (2001e). *Mojave 1998 06 (Jun)*, UNAVCO, Inc., GPS/GNSS Observations Dataset, doi:10.7283/T58G8HMF.

Miller, M. M., E. Humphreys, R. K. Dokka, and F. H. Webb (2001f). *Mojave 1998 12 (Dec)*, UNAVCO, Inc., GPS/GNSS Observations Dataset, doi:10.7283/T50Z715S.

Miller, M. M., E. Humphreys, R. K. Dokka, and F. H. Webb (2001g). *Garlock 1998/1999*, UNAVCO, Inc., GPS/GNSS Observations Dataset, doi:10.7283/T59G5JRT.

Miller, M. M., and D. J. Johnson (2001a). *Mojave 1999*, UNAVCO, Inc., GPS/GNSS Observations Dataset, doi:10.7283/T56Q1V5W.

Miller, M. M., and D. J. Johnson (2001b). *Mojave 2000*, UNAVCO, Inc., GPS/GNSS Observations Dataset, doi:10.7283/T5JW8BS7.

Miller, M. M., and D. J. Johnson (2001c). *Garlock 2000*, UNAVCO, Inc., GPS/GNSS Observations Dataset, doi:10.7283/T5KW5CXM.

Miller, M. M., and D. J. Johnson (2001d). *Mojave 2001 03 (Mar)*, UNAVCO, Inc., GPS/GNSS Observations Dataset, doi:10.7283/T5Z60KZ5.

Miller, M. M., and D. J. Johnson (2001e). *Garlock 2001 03 (Mar)*, UNAVCO, Inc., GPS/GNSS Observations Dataset, doi:10.7283/T5TD9V79.

Miller, M. M., and D. J. Johnson (2001f). *Mojave 2001 06 (Jun)*, UNAVCO, Inc., GPS/GNSS Observations Dataset, doi:10.7283/T5F769GJ.

Miller, M. M., and D. J. Johnson (2001g). *Garlock 2001 06 (Jun)*, UNAVCO, Inc., GPS/GNSS Observations Dataset, doi:10.7283/T5G44N6M.

Tymofyeyeva, E., and Y. Fialko (2015). *Mitigation of atmospheric phase delays in InSAR data, with application to the Eastern California Shear Zone*, J. Geophys. Res. Solid Earth **120** 5952–5963, doi:10.1002/2015JB011886.

UNAVCO Community (2019), *Ridgecrest California Earthquake Response 2019: Network of the Americas (NOTA) High Rate GNSS Data*, UNAVCO, Inc., GPS/GNSS Observations (Aggregation of Multiple Datasets), doi:10.7283/HZN1-5910.

U.S. Geological Survey and California Geological Survey (2006). *Quaternary fault and fold database for the United States*, accessed 2019-06-11, from USGS web site: https://earthquake.usgs.gov/hazards/qfaults/.

Wang, K., and R. Bürgmann (2019). *Co- and early postseismic deformation due to the 2019 Ridgecrest earthquake sequence constrained by Sentinel-1 and COSMO-SkyMed SAR data*, Seismol. Res. Lett., submitted.

Xu, X., and D. Sandwell (2019). *Coseismic displacements and surface fractures from Sentinel-1 InSAR: 2019 Ridgecrest earthquakes*, Seismol. Res. Lett., submitted.

Figures

Figure 1 (a) GNSS velocity solution, relative to North America (Altamimi et al., 2017), across the Mojave Desert region from GAGE products for continuous sites (red; Herring et al., 2016), SCEC's Crustal Motion Map for survey sites (blue; Shen et al., 2011, rotated from their Stable North America Reference Frame, SNARF, to the same Altamimi et al., 2017, definition of North America), and updated or new velocities for sites observed since by Funning (2016) and Funning et al. (2019a) within our region of interest (yellow; this study). Orange and green lines are mapped faults with evidence of displacement during the last 15 kyr and 130 kyr, respectively, from the USGS Quaternary Fault and Fold Database (USGS and CGS, 2006). The white line is the boundary of the NAWS China Lake. (b) The profile, centered at the intersection of the M_w6.4 and M_w7.1 surface ruptures, shows the velocity gradient (mostly profile-perpendicular, i.e., fault-parallel, shear) across the region.

Figure 2 Displacements of the July 4th, 2019, M_w6.4 Ridgecrest earthquake. Red vectors are for continuous sites and blue are for survey sites (four UCR installed within hours of the first earthquake). Yellow triangles show the five survey sites occupied by UCR after the M_w6.4 earthquake and hence during the M_w7.1 earthquake. The surface rupture is marked by the orange line (C. Milliner, pers. comm., via SCEC Response Forum at https://response.scec.org/) and the white line is the boundary of the NAWS China Lake, as in Figure 1. Displacements shown are listed in Table S1.

Figure 3 Displacements of the July 6th (5th, local time), 2019, M_w7.1 Ridgecrest earthquake. Vector colors and fault rupture for the first earthquake are as in Figure 2, with the M_w7.1 rupture in light orange. Green triangles are sites occupied by SIO/UCSD after the M_w7.1 earthquake and therefore do not have coseismic displacement estimates for this second earthquake separately from the first. Displacements shown are listed in Table S2.

Figure 4 Cumulative displacements from the two earthquakes combined. Vector colors and fault ruptures are as in Figure 3. Displacements shown are listed in Table S3.

Tables

***Table 1** Summary of GNSS surveys used to determine pre-earthquake positions for this study.*

Survey	**Citation**	**DOI**
Pre-earthquake velocity solution		
Mammoth/Mojave 1994	Miller et al. (1997)	10.7283/T57H1GGM
Mojave 1995	Miller et al. (1995)	10.7283/T5H12ZX8
Garlock 1997	Miller et al. (2001b)	10.7283/T55Q4T1H
Mojave 1997	Miller et al. (2001c)	10.7283/T5W66HPD
Garlock 1998 06 (Jun)	Miller et al. (2001d)	10.7283/T51Z4295
Mojave 1998 06 (Jun)	Miller et al. (2001e)	10.7283/T58G8HMF
Mojave 1998 12 (Dec)	Miller et al. (2001f)	10.7283/T50Z715S
Garlock 1998/1999	Miller et al. (2001g)	10.7283/T59G5JRT
Mojave 1999	Miller and Johnson (2001a)	10.7283/T56Q1V5W
Mojave 2000	Miller and Johnson (2001b)	10.7283/T5JW8BS7
Garlock 2000	Miller and Johnson (2001c)	10.7283/T5KW5CXM
Mojave 2001 03 (Mar)	Miller and Johnson (2001d)	10.7283/T5Z60KZ5
Garlock 2001 03 (Mar)	Miller and Johnson (2001e)	10.7283/T5TD9V79
Mojave 2001 06 (Jun)	Miller and Johnson (2001f)	10.7283/T5F769GJ
Garlock 2001 06 (Jun)	Miller and Johnson (2001g)	10.7283/T5G44N6M
GeoEarthScope 2005 (1)	Bevis and Hudnut (2005a)	10.7283/V5MV-QE58
GeoEarthScope 2005 (2)	Bevis and Hudnut (2005b)	10.7283/FQ3X-X311

San Jacinto Fault 2014	Funning (2016)	10.7283/T57H1GZW
Mojave 2019 (Feb)	Funning et al. (2019a)	10.7283/TFX5-EJ21
Mojave 2019 (Mar)	Funning et al. (2019a)	10.7283/TFX5-EJ21
Ridgecrest (UCSD)	Fialko et al. (2019a)	10.7283/N74Q-GA66
Post-Ridgecrest (UCSD)	Fialko et al. (2019b)	10.7283/YJK0-B215
Post-Ridgecrest (UCR)	Funning et al. (2019b)	10.7283/5ASB-9V26

Figure 1

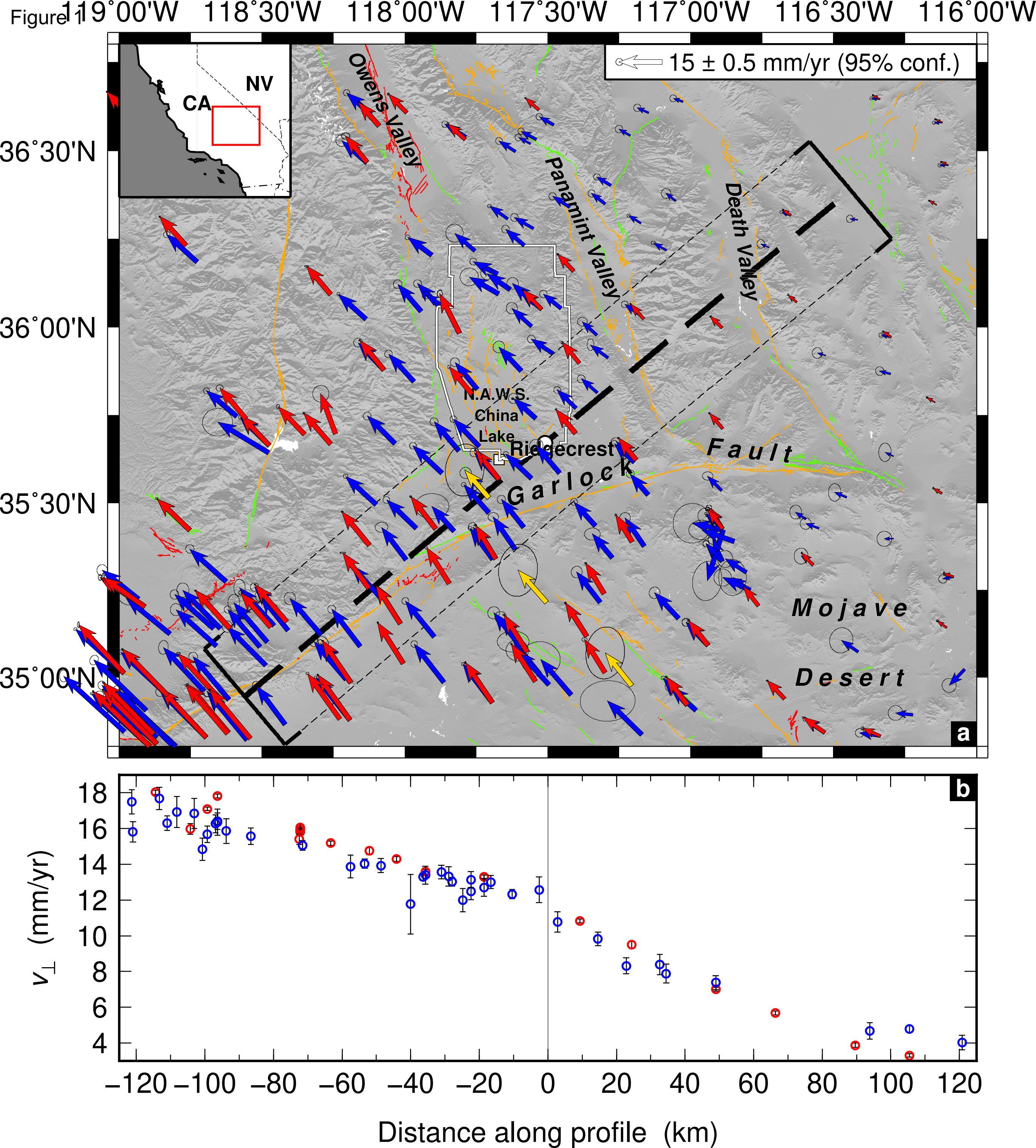

119°00'W
118°30'W
118°00'W
117°30'W
117°00'W
116°30'W
116°00'W
36°30'N
36°00'N
35°30'N
35°00'N
CA
NV
15 ± 0.5 mm/yr (95% conf.)
Owens Valley
Panamint Valley
Death Valley
N.A.W.S. China Lake
Ridgecrest
Garlock
Fault
Mojave
Desert
a
b
$v_\perp$ (mm/yr)
Distance along profile (km)

Figure 2

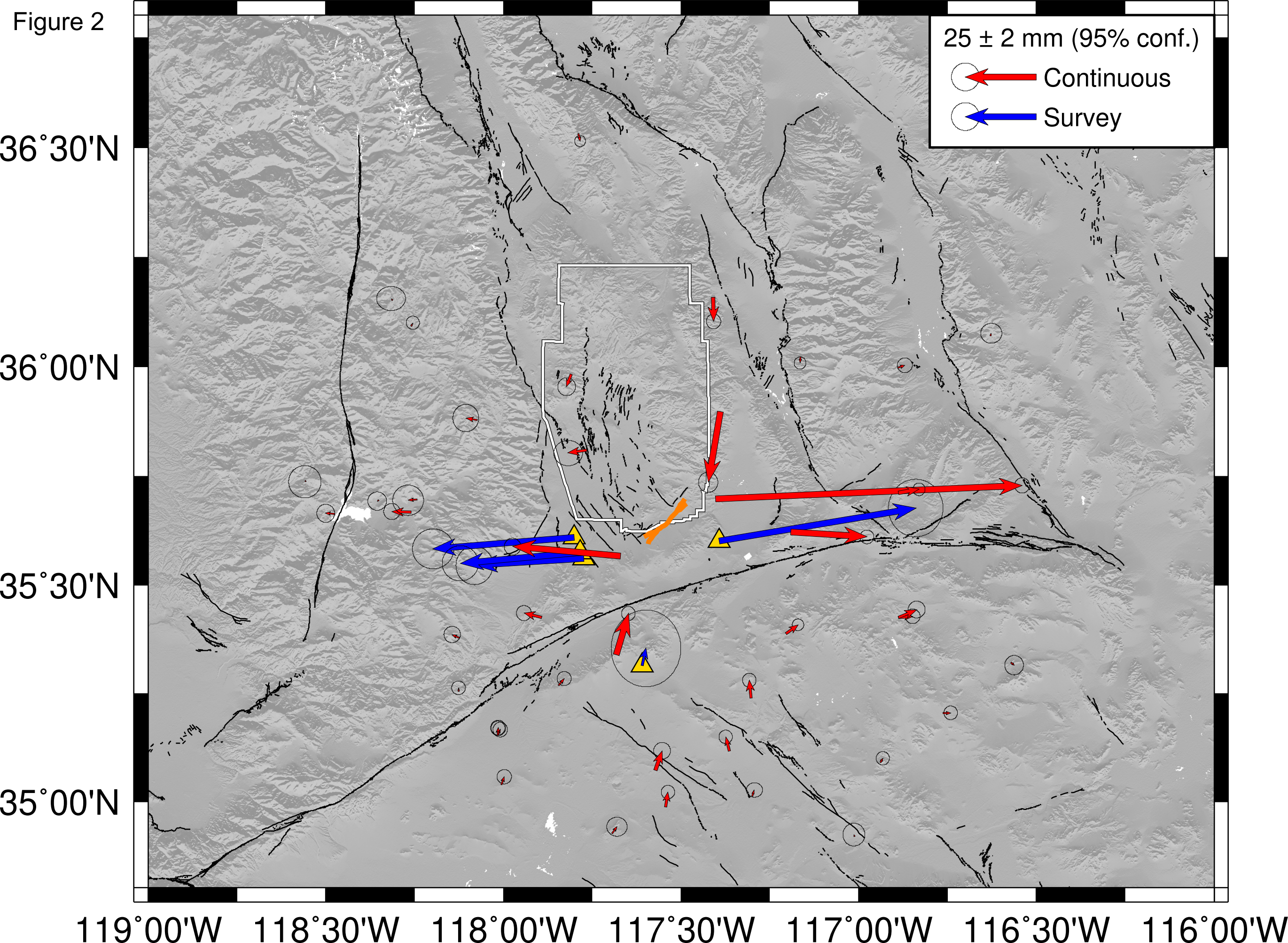
25 ± 2 mm (95% conf.)
Continuous
Survey
36˚30'N
36˚00'N
35˚30'N
35˚00'N
119˚00'W
118˚30'W
118˚00'W
117˚30'W
117˚00'W
116˚30'W
116˚00'W

Figure 3

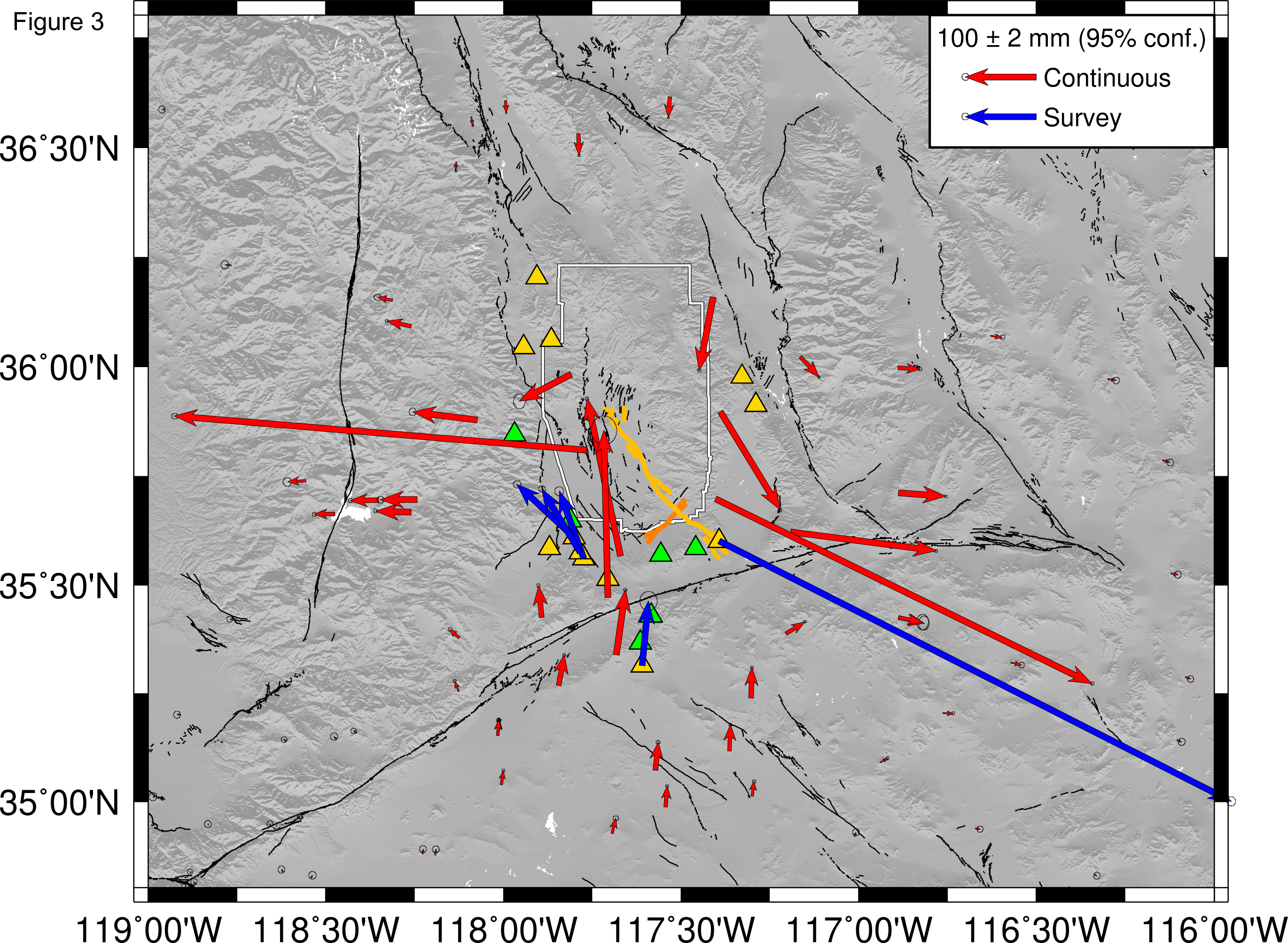
100 ± 2 mm (95% conf.)
Continuous
Survey
36°30'N
36°00'N
35°30'N
35°00'N
119°00'W
118°30'W
118°00'W
117°30'W
117°00'W
116°30'W
116°00'W

Figure 4

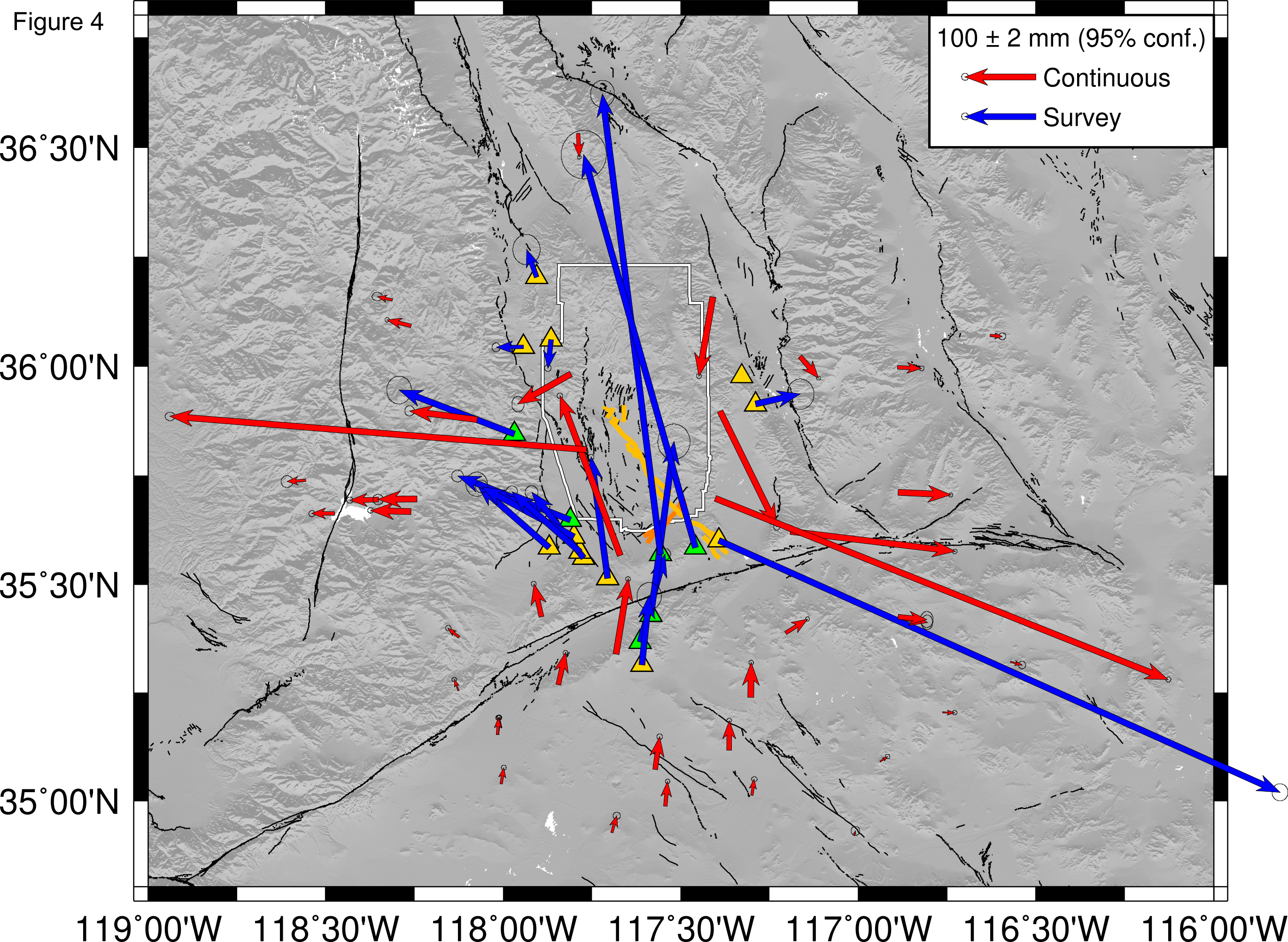

100 ± 2 mm (95% conf.)
Continuous
Survey
36˚30'N
36˚00'N
35˚30'N
35˚00'N
119˚00'W
118˚30'W
118˚00'W
117˚30'W
117˚00'W
116˚30'W
116˚00'W

Survey and Continuous GNSS in the vicinity of the July 2019 Ridgecrest earthquakes

Michael Floyd, Gareth Funning, Yuri Fialko, Rachel Terry, Thomas Herring

Supplemental Material

The supplemental material consists of three figures and three plain text tables.

Figure S1 Summary of the occupation times for survey sites during the (a) February and (b) March 2019 surveys conducted in the region of the July 2019 earthquakes. The resulting position uncertainties are approximately 1.5–2.1 mm in the horizontal components (see main text for details).

Figure S2 Summary of first survey observations during the post-earthquake response. Blue IDs are survey sites occupied by the UCR field team and gold IDs are survey sites occupied by the SIO/UCSD field team.

Figure S3 Photographs of five survey sites demonstrating the type of monuments observed during the field response. (a) A threaded rod set in a concrete block at GS04; (b) A bronze disk on end of a metal pipe at BM25; (c) An aluminum disk on driven rod inside a protective pipe at V511; (d) A stainless steel pin cemented into a rock outcrop at ground level at PNCL; and (e) A bronze disk set in the top of a buried concrete pillar at H701. All photographs courtesy of Gareth Funning (UCR).

Table S1 Coseismic displacements due to the first, M_w6.4 earthquake. “Lon.” is longitude (°E), “Lat.” is latitude (°N), “de” is the estimated east displacement, “dn” is the estimated north displacement, “se” is the one-sigma formal uncertainty associated with the east displacement, “sn” is the one-sigma formal uncertainty associated with the north displacement, “rho” is the correlation coefficient between the east and north displacements, and “Site” is the four-character site ID.

Table S2 Coseismic displacements due to the second, M_w7.1 earthquake. “Lon.” is longitude (°E), “Lat.” is latitude (°N), “de” is the estimated east displacement, “dn” is the estimated north displacement, “se” is the one-sigma formal uncertainty associated with the east displacement, “sn” is the one-sigma formal uncertainty associated with the north displacement, “rho” is the correlation coefficient between the east and north displacements, and “Site” is the four-character site ID.

Table S3 Cumulative displacements due to both earthquakes combined. “Lon.” is longitude (°E), “Lat.” is latitude (°N), “de” is the estimated east displacement, “dn” is the estimated north displacement, “se” is the one-sigma formal uncertainty associated with the east displacement, “sn” is the one-sigma formal uncertainty associated with the north displacement, “rho” is the correlation coefficient between the east and north displacements, and “Site” is the four-character site ID.

Figure

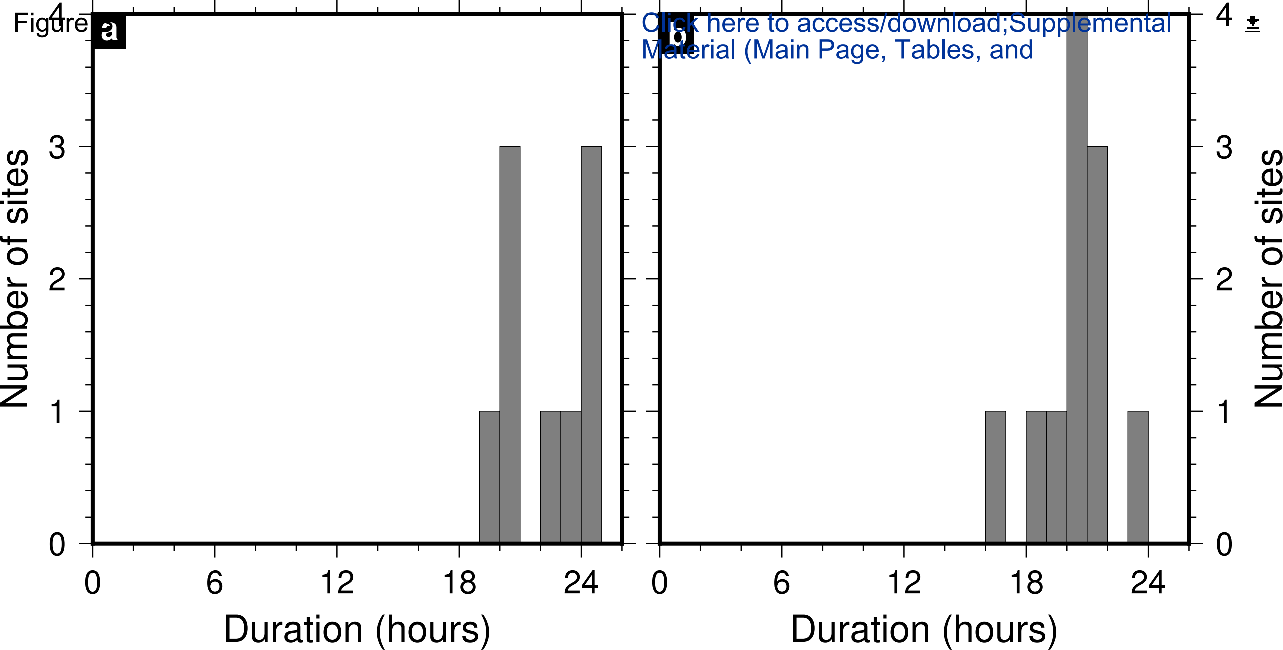
a
b
Number of sites
0
1
2
3
4
Duration (hours)
0
6
12
18
24
Number of sites
Duration (hours)

Figure S2

Click here to access/download;Supplemental Material (Main Page, Tables, and

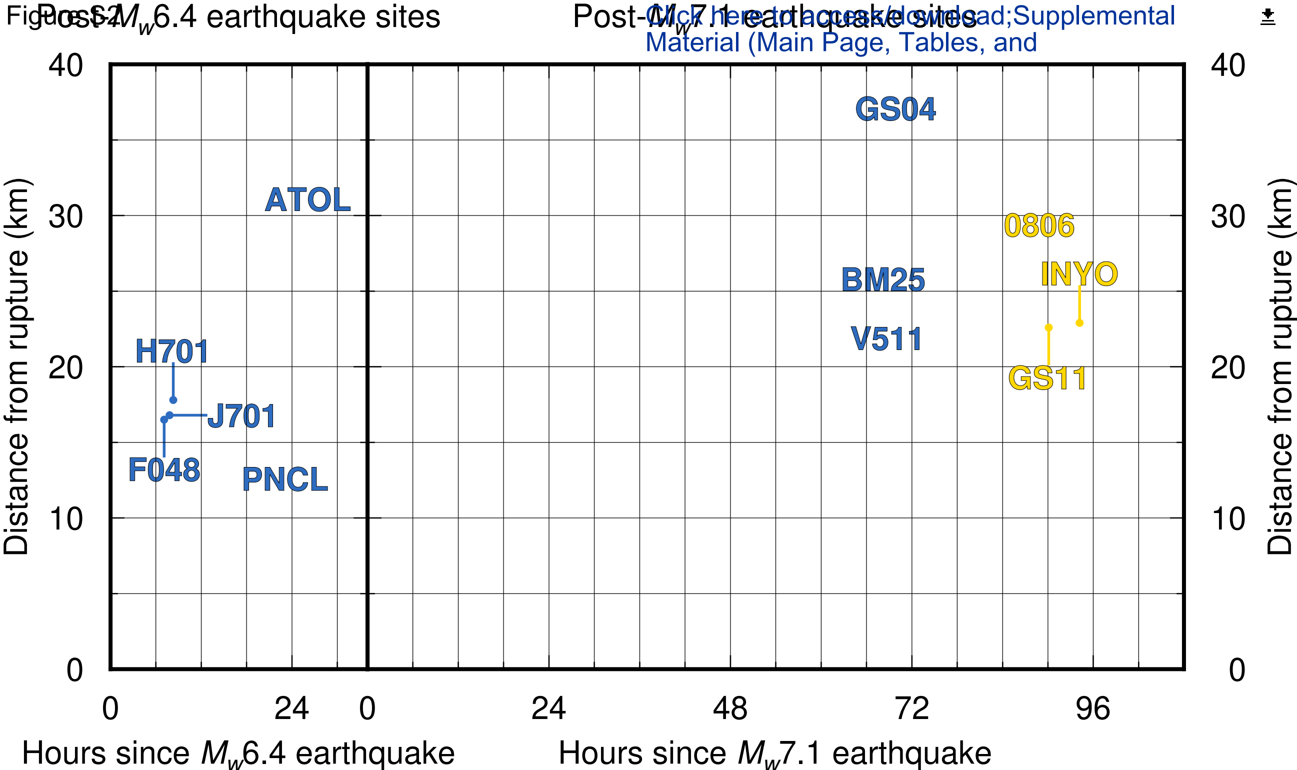

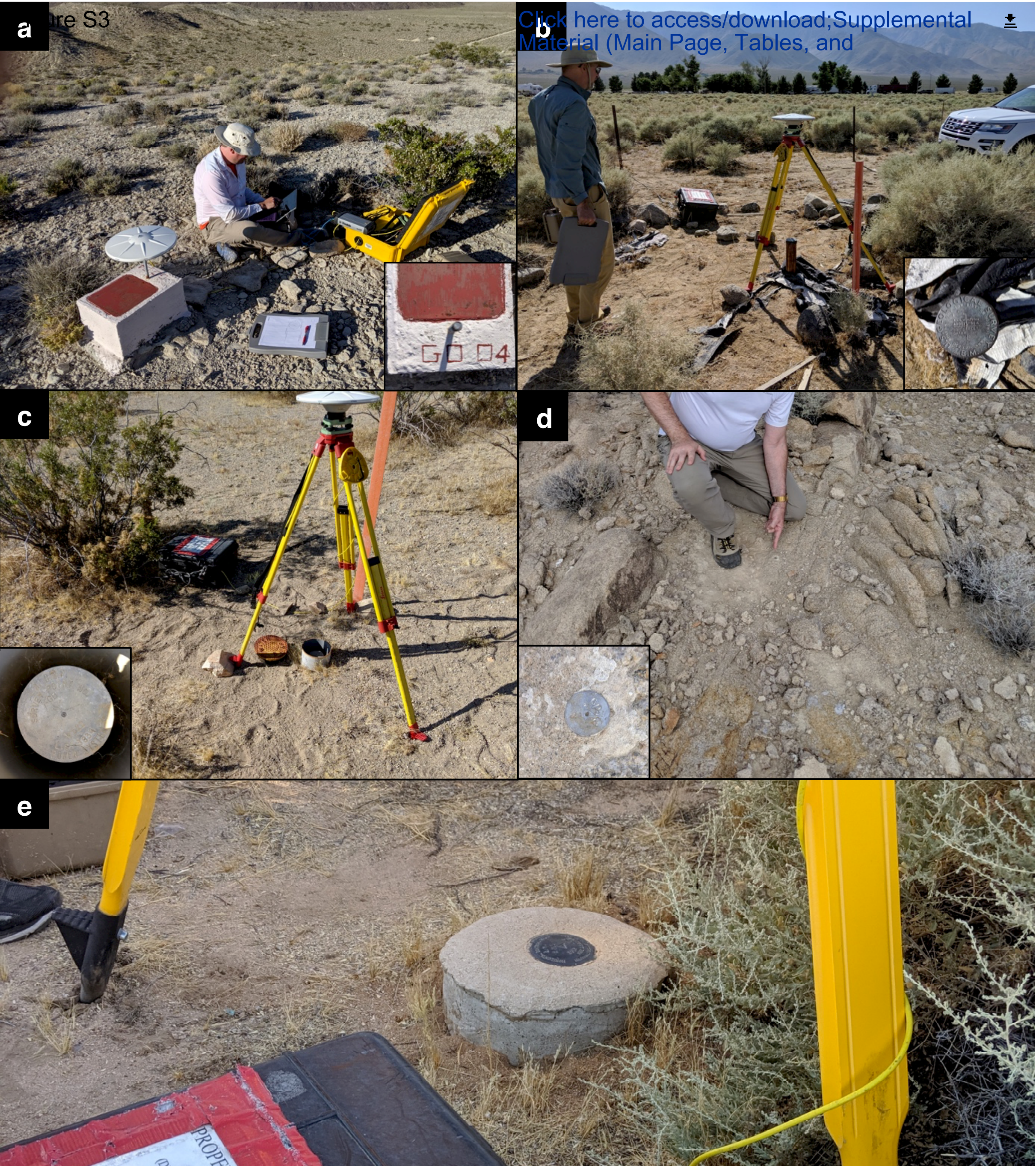
ure S3
a
b
c
d
e

Table S1

Click here to access/download;Supplemental Material (Main Page, Tables, and Figures);TableS1.txt

1234567890123456789012345678901234567890123456789012345678901234567890123

Lon.	Lat.	de(mm)	dn(mm)	se(mm)	sn(mm)	rho	Site
Survey sites (UCR)							
242.39061	35.31314	1.25	6.05	5.01	5.51	0.001	ATOL
242.22535	35.56001	-1.03	-0.56	27.25	27.25	0.001	F048
242.19954	35.60910	-16.16	-25.87	9.06	9.06	0.001	H701
242.21612	35.57474	-17.63	-4.44	4.06	4.00	0.001	J701
242.60639	35.60077	-876.63	76.00	66.94	66.83	0.001	PNCL
Continuous sites							
241.92590	35.87839	-4.01	0.66	1.86	1.97	0.001	BEPK
242.98800	34.91861	-0.22	0.66	1.58	1.63	0.001	BSRY
242.32882	35.56531	-39.07	1.80	1.19	1.21	0.001	CCCC
242.19111	35.98234	-3.22	-6.57	1.28	1.29	0.001	COSO
242.42697	35.07173	1.02	4.92	1.21	1.20	0.001	CPBN
242.15412	35.26746	1.96	2.31	1.01	1.01	0.001	DTPG
243.11075	35.42516	4.42	-0.59	1.07	1.05	0.001	GOL2
243.11075	35.42516	5.01	0.66	1.22	1.21	0.001	GOLD
242.70079	35.01154	0.59	2.12	1.17	1.04	0.001	HAR7
241.52570	35.66227	-3.64	-0.27	1.28	1.30	0.001	ISLK
243.06035	35.09020	0.13	0.39	0.95	0.96	0.001	LNMT
243.37129	36.07132	0.10	0.68	1.52	1.43	0.001	P462
242.83532	36.02246	-0.73	-3.08	0.85	0.87	0.001	P463
242.59000	36.15905	0.03	-8.71	1.03	1.07	0.001	P464
242.21054	36.53125	0.29	-3.13	0.78	0.81	0.001	P466
241.87348	35.25431	-0.55	0.46	0.99	0.97	0.001	P568
241.87623	35.37797	-3.24	0.16	1.19	1.17	0.001	P569
241.73996	35.66735	-7.39	-0.76	1.17	1.16	0.001	P570
241.73950	36.09309	0.27	0.58	0.95	0.95	0.001	P573
241.99423	35.03876	0.37	1.87	1.04	1.03	0.001	P579
242.80777	35.62095	26.15	-2.74	0.99	0.99	0.001	P580
242.45660	34.98700	0.18	4.40	0.97	0.97	0.001	P583
242.63525	35.11678	-1.38	4.74	0.96	0.97	0.001	P590
241.98352	35.15242	-0.43	1.83	1.00	1.00	0.001	P591
242.69677	35.23855	-1.36	5.26	0.98	0.99	0.001	P592
242.79494	35.38787	3.59	2.11	0.83	0.84	0.001	P593
242.60986	35.89671	-4.26	-24.78	1.39	1.45	0.001	P594
242.59716	35.69756	107.17	3.39	1.08	1.10	0.001	P595
243.11048	35.99818	1.54	-0.38	1.08	1.06	0.001	P596
243.11160	35.71060	6.72	0.56	0.88	0.91	0.001	P597
243.23709	35.20461	2.13	-0.74	0.98	0.98	0.001	P615
242.10666	35.42456	-6.74	0.69	1.07	1.09	0.001	P616
243.42835	35.32064	1.10	-0.90	1.34	1.40	0.001	P617
241.98339	35.15243	0.57	1.53	1.04	1.06	0.001	P811
241.98346	35.15250	0.10	2.53	1.08	1.10	0.001	P812
242.30552	34.92542	1.22	1.70	1.47	1.37	0.001	PHLB
242.31665	35.33871	3.52	13.37	0.99	1.01	0.001	RAMT
242.23510	35.80856	-6.81	-1.26	2.07	1.82	0.001	TOWG
241.44302	35.73839	-0.29	-0.30	2.33	2.32	0.001	WASG
241.64804	35.69505	-0.53	-0.55	1.35	1.32	0.001	WHFG
241.68689	36.15211	-0.40	0.57	2.08	1.73	0.001	WLHG

```
  241.75761  35.69557   -3.31   -0.30   2.22   2.18  0.001 WORG
12345678901234567890123456789012345678901234567890123456789012
```

Table S2

1234567890123456789012345678901234567890123456789012345678901234567890123

Lon.	Lat.	de(mm)	dn(mm)	se(mm)	sn(mm)	rho	Site
Survey sites (UCR)							
242.39061	35.31314	8.67	90.88	4.97	5.49	0.001	ATOL
242.22535	35.56001	-33.88	94.93	2.60	2.63	0.001	F048
242.19954	35.60910	-77.40	72.51	2.38	2.27	0.001	H701
242.21612	35.57474	-46.61	88.59	2.14	2.05	0.001	J701
242.60640	35.60077	715.61	-366.11	2.47	2.74	0.001	PNCL
Continuous sites							
241.08944	35.20126	-4.14	-0.58	1.96	2.05	0.001	ARM2
241.92590	35.87839	-90.82	11.46	2.04	2.16	0.001	BEPK
243.91957	35.28705	6.99	-2.49	1.79	1.90	0.001	BKAP
242.98800	34.91861	1.98	6.01	1.95	2.05	0.001	BSRY
242.32882	35.56531	-47.17	221.40	1.09	1.10	0.001	CCCC
243.66407	34.82947	3.05	-1.10	1.94	2.01	0.001	CDMT
242.19111	35.98234	-73.45	-38.32	3.35	4.26	0.001	COSO
242.42697	35.07174	3.21	38.22	1.11	1.10	0.001	CPBN
242.15412	35.26746	7.97	42.61	0.90	0.89	0.001	DTPG
241.16959	34.94619	-0.84	0.73	1.99	2.07	0.001	EDPP
241.10662	34.80019	-1.09	3.13	2.15	2.22	0.001	FZHS
243.11075	35.42516	35.86	-8.69	3.07	4.05	0.001	GOL2
243.11075	35.42516	34.11	-7.08	3.38	4.47	0.001	GOLD
242.70079	35.01154	2.09	20.48	1.08	0.95	0.001	HAR7
241.52570	35.66227	-29.72	-1.35	1.21	1.23	0.001	ISLK
241.13226	34.80752	-1.84	3.65	1.84	1.90	0.001	LJRN
243.06035	35.09020	9.39	4.89	0.88	0.88	0.001	LNMT
242.46846	36.61432	-2.47	-29.51	0.47	0.49	0.001	P091
242.00585	36.60602	0.32	-18.22	0.49	0.51	0.001	P093
243.37129	36.07132	16.41	-2.73	1.42	1.33	0.001	P462
242.83533	36.02246	25.93	-28.75	0.75	0.75	0.001	P463
242.59000	36.15904	-19.96	-103.42	0.94	0.96	0.001	P464
241.86756	36.46683	-1.71	-13.38	0.54	0.54	0.001	P465
242.21054	36.53125	0.52	-31.32	0.70	0.72	0.001	P466
241.90937	36.57020	1.80	-13.07	0.59	0.58	0.001	P467
241.12103	34.83509	-1.67	1.03	1.57	1.60	0.001	P553
241.34441	34.94439	-0.79	2.08	1.75	1.83	0.001	P557
241.38834	35.13861	-2.92	2.54	1.66	1.74	0.001	P558
241.45913	34.82181	1.54	4.05	2.12	2.20	0.001	P560
241.24642	35.42095	-8.73	-0.05	1.61	1.72	0.001	P567
241.87348	35.25431	-6.07	13.70	0.88	0.87	0.001	P568
241.87623	35.37797	-13.48	10.95	1.07	1.05	0.001	P569
241.73996	35.66735	-50.65	0.62	1.08	1.07	0.001	P570
241.23328	36.23137	-8.74	1.06	2.23	2.34	0.001	P571
241.04540	36.58552	-3.35	0.34	1.91	2.02	0.001	P572
241.73950	36.09309	-34.40	6.57	0.87	0.86	0.001	P573
241.99423	35.03876	2.12	19.14	0.94	0.93	0.001	P579
242.80777	35.62095	204.62	-26.69	0.88	0.87	0.001	P580
242.45660	34.98700	1.76	28.85	0.88	0.88	0.001	P583
242.63525	35.11678	1.32	36.59	0.87	0.88	0.001	P590
241.98352	35.15243	2.23	20.98	0.91	0.91	0.001	P591

242.69677	35.23855	0.96	42.44	0.87	0.87	0.001	P592
242.79494	35.38787	26.33	16.12	0.75	0.76	0.001	P593
242.60987	35.89671	83.96	-138.19	1.06	1.08	0.001	P594
242.59717	35.69756	529.74	-260.33	0.98	0.99	0.001	P595
243.11048	35.99818	31.01	-3.03	0.96	0.95	0.001	P596
243.11160	35.71060	66.50	-5.21	0.78	0.80	0.001	P597
243.32854	34.93683	6.39	-0.70	1.74	1.83	0.001	P604
243.23709	35.20461	13.74	-1.46	0.88	0.88	0.001	P615
242.10666	35.42456	-4.62	44.54	0.97	0.99	0.001	P616
243.42835	35.32064	15.03	-3.47	1.59	1.68	0.001	P617
243.89607	35.14189	6.41	-2.45	2.01	2.10	0.001	P618
243.87820	35.52595	10.13	-1.59	1.95	2.08	0.001	P619
243.85508	35.78536	10.88	-2.90	1.86	1.97	0.001	P620
241.37854	34.83602	-1.65	3.55	2.00	2.08	0.001	P808
241.98339	35.15243	1.08	21.64	0.95	0.96	0.001	P811
241.98346	35.15250	0.81	20.70	0.97	0.99	0.001	P812
242.30552	34.92542	4.55	20.49	1.54	1.45	0.001	PHLB
242.31665	35.33872	12.74	90.83	0.91	0.92	0.001	RAMT
241.80707	34.87508	1.25	8.24	1.96	2.03	0.001	RSTP
243.70101	35.97134	11.80	-1.58	1.85	1.95	0.001	SHOS
241.53020	35.14306	-3.69	4.20	2.06	2.16	0.001	TEHA
241.58543	35.15818	-3.67	2.99	1.50	1.59	0.001	THCP
242.23510	35.80856	-580.29	47.78	1.85	1.65	0.001	TOWG
241.77142	34.87886	1.11	6.38	1.94	2.04	0.001	TPOG
241.44302	35.73839	-25.96	-1.65	2.48	2.52	0.001	WASG
241.01631	35.01085	-1.63	0.01	2.33	2.40	0.001	WGPP
241.64804	35.69505	-39.97	-1.07	1.25	1.22	0.001	WHFG
241.68689	36.15211	-20.51	4.00	2.06	1.70	0.001	WLHG
241.75761	35.69557	-52.16	-0.61	2.03	2.03	0.001	WORG

1234567890123456789012345678901234567890123456789012345678901234567890123

Table S3

12345678901234567890123456789012345678901234567890123456789012345

Lon.	Lat.	de(mm)	dn(mm)	se(mm)	sn(mm)	rho	Site
Survey sites (UCR)							
242.39061	35.31314	9.92	96.93	7.06	7.78	0.001	ATOL
242.22535	35.56001	-34.91	94.37	27.37	27.38	0.001	F048
242.19954	35.60910	-93.56	46.64	9.37	9.34	0.001	H701
242.21612	35.57474	-64.24	84.15	4.59	4.49	0.001	J701
242.60639	35.60077	-161.02	-290.11	66.99	66.89	0.001	PNCL
242.05597	36.04457	-44.84	-10.30	2.28	2.62	0.001	BM25
242.09341	36.20353	-28.21	17.88	7.85	8.70	0.001	GS04
242.29350	35.47029	-18.06	216.75	7.38	8.32	0.001	GS16
242.12967	35.58376	-114.83	70.85	6.22	6.99	0.001	GS18
242.71087	35.91323	49.95	-4.82	7.74	8.75	0.001	GS25
242.29363	35.51302	-26.29	166.32	1.60	1.69	0.001	PASO
242.13432	36.06142	-9.33	-47.25	1.85	1.94	0.001	V511
Survey sites (SIO/UCSD)							
242.38579	35.36616	22.38	105.18	3.02	3.19	0.001	0806
242.41515	35.42877	20.07	225.56	9.26	10.23	0.001	GS11
242.44323	35.56940	-94.50	629.58	6.89	7.77	0.001	GS17
242.03051	35.84526	-174.38	43.23	7.09	8.00	0.001	GS22
242.54108	35.58429	-170.04	534.68	12.95	13.97	0.001	GS48
242.18819	35.64738	-145.16	-19.70	124.61	124.37	0.001	INYO
Continuous sites							
241.92590	35.87839	-94.83	12.12	2.76	2.92	0.001	BEPK
242.98800	34.91861	1.76	6.67	2.51	2.62	0.001	BSRY
242.32882	35.56531	-86.24	223.20	1.61	1.64	0.001	CCCC
242.19111	35.98234	-76.67	-44.89	3.59	4.45	0.001	COSO
242.42697	35.07173	4.23	43.14	1.64	1.63	0.001	CPBN
242.15412	35.26746	9.93	44.92	1.35	1.35	0.001	DTPG
243.11075	35.42516	40.28	-9.28	3.25	4.18	0.001	GOL2
243.11075	35.42516	39.12	-6.42	3.59	4.63	0.001	GOLD
242.70079	35.01154	2.68	22.60	1.59	1.41	0.001	HAR7
239.59761	35.88081	-3.18	0.49	2.14	2.28	0.001	HUNT
241.52570	35.66227	-33.36	-1.62	1.76	1.79	0.001	ISLK
243.06035	35.09020	9.52	5.28	1.29	1.30	0.001	LNMT
243.37129	36.07132	16.51	-2.05	2.08	1.95	0.001	P462
242.83532	36.02246	25.20	-31.83	1.13	1.15	0.001	P463
242.59000	36.15905	-19.93	-112.13	1.39	1.44	0.001	P464
242.21054	36.53125	0.81	-34.45	1.05	1.08	0.001	P466
241.87348	35.25431	-6.62	14.16	1.32	1.30	0.001	P568
241.87623	35.37797	-16.72	11.11	1.60	1.57	0.001	P569
241.73996	35.66735	-58.04	-0.14	1.59	1.58	0.001	P570
241.73950	36.09309	-34.13	7.15	1.29	1.28	0.001	P573
241.99423	35.03876	2.49	21.01	1.40	1.39	0.001	P579
242.80777	35.62095	230.77	-29.43	1.32	1.32	0.001	P580
242.45660	34.98700	1.94	33.25	1.31	1.31	0.001	P583
242.63525	35.11678	-0.06	41.33	1.30	1.31	0.001	P590
241.98352	35.15242	1.80	22.81	1.35	1.35	0.001	P591

242.69677	35.23855	-0.40	47.70	1.31	1.32	0.001	P592
242.79494	35.38787	29.92	18.23	1.12	1.13	0.001	P593
242.60986	35.89671	79.70	-162.97	1.75	1.81	0.001	P594
242.59716	35.69756	636.91	-256.94	1.46	1.48	0.001	P595
243.11048	35.99818	32.55	-3.41	1.44	1.42	0.001	P596
243.11160	35.71060	73.22	-4.65	1.18	1.21	0.001	P597
243.23709	35.20461	15.87	-2.20	1.32	1.32	0.001	P615
242.10666	35.42456	-11.36	45.23	1.44	1.47	0.001	P616
243.42835	35.32064	16.13	-4.37	2.08	2.19	0.001	P617
241.98339	35.15243	1.65	23.17	1.41	1.43	0.001	P811
241.98346	35.15250	0.91	23.23	1.45	1.48	0.001	P812
242.30552	34.92542	5.77	22.19	2.13	1.99	0.001	PHLB
242.31665	35.33871	16.26	104.20	1.34	1.37	0.001	RAMT
242.23510	35.80856	-587.10	46.52	2.78	2.46	0.001	TOWG
241.44302	35.73839	-26.25	-1.95	3.40	3.43	0.001	WASG
241.64804	35.69505	-40.50	-1.62	1.84	1.80	0.001	WHFG
241.68689	36.15211	-20.91	4.57	2.93	2.43	0.001	WLHG
241.75761	35.69557	-55.47	-0.91	3.01	2.98	0.001	WORG

1234567890123456789012345678901234567890123456789012345678901234567890123